Ocean Engineering 312 (2024) 119026

Contents lists available at ScienceDirect

Ocean Engineering

journal homepage: www.elsevier.com/locate/oceaneng

Research paper

Numerical investigations of breaking waves and air entrainment induced by a shallowly submerged hydrofoil

Yuming Shao [a], Wentao Wang [a,b], Decheng Wan [a], Jianhua Wang [a,*]

[a] Computational Marine Hydrodynamics Lab (CMHL), School of Ocean and Civil Engineering, Shanghai Jiao Tong University, Shanghai 200240, China
[b] China Ship Scientific Research Center, Wuxi 214082, China

ARTICLE INFO

Keywords:
Free-surface flows
Submerged hydrofoil
Wave breaking
Air entrainment
Bubble dynamics
Vortex interactions

ABSTRACT

Wave breaking is an expression of the intense interaction of two-phase flow interfaces, involving numerous physical phenomena and mechanisms. It holds significant importance in the marine and ocean engineering fields. This study investigates the flow around a shallowly submerged hydrofoil at six different submergence depths ($h/c = 0.3, 0.5, 0.7, 0.9, 1.1$ and 1.3). The primary focus is to reveal the impact of submergence depth on the flow field around the hydrofoil and the deformation of the free surface. By comparing the kinetic and potential energy fluxes for the conditions of $h/c = 0.3, 0.5,$ and 0.7, we find that energy dissipation for these three conditions is 5.35%, 4.21%, and 3.42%, respectively. Furthermore, by extracting the spatial-temporal characteristics of bubbles, we analyze the issues of air entrainment caused by free surface breaking and identify three distinct types of air entrainment. It is observed that at lower submergence depths, all three types coexist, with Type-I entrainment being the main source of bubble volume. At higher submergence depths, only Type-III entrainment occurs, which causes bubbles to be swept to deeper water. These bubbles swept down remain in the water for a longer duration and exhibit a more widespread distribution.

1. Introduction

Wave breaking and air entrainment are widely present phenomena in nature, crucial processes in upper ocean dynamics and air-sea interactions, and regarded as primary mechanisms for oceanic energy dissipation (Deike, 2022). During the evolution of waves, when wave crests reach their maximum height, surface instabilities occur leading to wave face collapse and entrainment of air into the water column. This phenomenon holds particular significance in the field of marine engineering, as wave breaking results in additional propulsion energy consumption and the generation of extensive white foam behind ships (Li et al., 2022). Moreover, shipborne radar systems are obstructed by sweep-down bubbles (Mallat al., 2018), offshore platform columns and subdecks experience wave impacts, and nearshore structures are influenced by shallow water wave breaking (Choi et al., 2015). At present, a growing number of scholars are focusing on this phenomenon. However, researching this phenomenon is still challenging because of the intricacy of wave breaking mechanisms and the turbulence that follows breaking.

Laboratory experiments are currently an important means of studying wave breaking phenomena. Some scholars use high-definition cameras and acoustic instruments to delve into the instability and mechanisms of wave breaking (Deane and Stokes, 2002; Blenkinsopp and Chaplin, 2010; Erinin et al., 2023a; 2023b). They argue that the size distribution of bubble clusters generated by wave breaking follows a power-law distribution. Bubbles larger than the Hinze scale undergo turbulent shear fragmentation, with a power exponent of $-10/3$. Bubbles smaller than the Hinze scale are dominated by flow instability induced by surface tension, with a power exponent of $-3/2$. However, detailed analysis is difficult due to the transitory, stochastic, and uncertain nature of wave breaking processes, which presents substantial obstacles to experimental observations (Hu et al., 2023). With the advancement of computer performance and numerical methods, studying this phenomenon through numerical simulation techniques becomes feasible. Nevertheless, capturing small-scale structures such as bubbles and droplets during the breaking process still requires a large number of grids. Wang et al. (2016) conducted high-fidelity numerical simulations of wave breaking, effectively capturing small-scale structures such as air entrainment and droplet splashing. However, they employed uniform grids, resulting in a total of 12 billion grid points, which entails a significant waste of computational resources. Adaptive mesh refinement

* Corresponding author.
E-mail address: jianhuawang@sjtu.edu.cn (J. Wang).

https://doi.org/10.1016/j.oceaneng.2024.119026
Received 11 June 2024; Received in revised form 30 July 2024; Accepted 16 August 2024
Available online 24 August 2024

(AMR) effectively addresses this issue by adaptively refining and coarsening grids based on changes in physical quantities. Mostert et al. (2022) used the DNS method to simulate turbulence, bubble, and droplet generation during breaking under different Reynolds and Bond numbers. With the AMR scheme, they reduced the grid from approximately 8.6 billion to 150 million, greatly alleviating the computational burden. Therefore, employing AMR technology to capture wave breaking and air entrainment is a more appropriate choice.

For wave breaking phenomena induced by structures, two conditions can be distinguished based on the position of the structure: piercing the free surface and completely submerged. In the first condition, the most common condition in the marine domain is ship bow wave breaking (Olivieri et al., 2003, 2007; Carrica et al., 2010; Wang et al., 2020). Wu and Taylor (1995) utilized the delayed detached eddy simulation (DDES) method to compare the bow breaking waves of the DTMB ship model under three different bow trim conditions. The results indicate that increasing the bow trim angle sharpens the bow wave's free surface and increases wave amplitude. They analyzed the force and motion of ships due to breaking waves from a macroscopic point of view. However, due to grid limitations, they did not further analyze the structures such as bubbles and droplets caused by breaking waves. Hu et al. (2021, 2023) simplified the bow into a flat plate and conducted refined numerical simulations of wave breaking and wake characteristics of the plate towing using the adaptive block-structured grid refinement solver BAMR-SJTU. They analyzed the flow structure of plate wave breaking, including the evolution of the free surface and characteristics of various breaking wave forms. Additionally, due to air entrainment and cavity collapse, a large number of bubbles are generated below the free surface. These bubbles are numerous, have a wide range of radius, and continuously change over time. Therefore, they also delved into the evolution characteristics of underwater bubble clusters and the size distribution properties of bubbles under different flow attack angles. They also did similar simulations for the surface-piercing hydrofoil (Li et al., 2021) and the transom stern ship (Yang et al., 2023).

When a uniform flow passes over a completely submerged structure, the influence of the structure leads to a quasi-stable mechanism in the wake behind the structure, characterized by regular wave pulsations (Sheridan et al., 1997). Moreover, as the structure approaches the free surface or undergoes motion, the waves at the free surface become steeper and eventually break. The simplest blunt-body structure, the cylinder, has been extensively studied, with a primary focus on issues such as the forces acting on the cylinder and the vorticity field (Barkley and Henderson, 1996; Centiner et al., 2001; Rao et al., 2013). Colagrossi et al. (2019) extensively studied the dynamics of the free surface induced by a submerged horizontal cylinder using three methods: Smoothed Particle Hydrodynamic method (SPH), Finite Volume scheme with a Level-Set algorithm (LS-FVM), and Finite Volume scheme with a Volume-of-Fluid algorithm (VOF-FVM). They provided abundant data to serve as benchmark cases for other solvers. Hendrickson and Yue (2019, 2022) employed the DNS method to investigate the initial entrainment induced by a submerged cylinder on the free surface and established a mathematical entrainment model to describe the volume entrainment caused by the interaction between surface-parallel vorticity rise and the air-water interface in quasi-two-dimension. Guo et al. (2023) captured the air entrainment induced by a rotating cylinder under two-dimensional conditions. They found that entrainment can be classified into two types: vortex entrainment caused by the parallel free surface and wake jet entrainment. For wake jet entrainment, the accompanying bubbles have a more widespread distribution in space.

Duncan (1983) was among the first to experimentally measure surface-height profiles and vertical distributions of velocity and total head of NACA0012 hydrofoil wakes under various water depth conditions. Their findings revealed that the hydrofoil's resistance could be divided into two parts: one associated with the turbulent breaking region and the other with the non-breaking waves in the wake. Under breaking wave conditions, the hydrofoil's resistance could reach up to three times that calculated theoretically under non-breaking wave conditions. Subsequently, several scholars (Miller et al., 1999; Kang et al., 2012) conducted experiments to study the turbulent characteristics and variations in free surface height in the breaking wave region. Murai et al. (2020) conducted experiments by installing a hydrofoil to a ship model, utilizing the bubble generation characteristics of the hydrofoil for power-saving purposes. They identified three different multiphase flow modes of bubble generation and found that the volumetric flow rate of the generated bubbles increased with the ship speed, with a power greater than two. In numerical simulations, early nonlinear potential flow boundary integral methods and boundary element methods were widely used to define pressure distributions to represent the effects of wave breaking (Kennell et al., 1984; Wu and Taylor, 1995). However, these methods could only partially reflect the evolution of the wave surface and the flow field below the free surface, failing to capture the strong nonlinear characteristics generated after wave breaking. Recently, using multiphase flow solvers has become the mainstream approach to studying this problem (Ali and Karim, 2010; Karim et al., 2014). Pernod et al. (2023) utilized the commercial software FINE/-Marine combined with Unsteady Reynolds Averaged Navier-Stokes (URANS) to investigate the behavior of a NACA0012 hydrofoil at 5-degree angle of attack under different submergence depths. They examined the hydrofoil's lift and drag variations and emphasized the significance of taking limiting water depth into account. Ni et al. (2019, 2021) studied the effect of attack angle on the hydrodynamic performance of slotted hydrofoils. They found that, compared to a baseline case, the maximum lift coefficient of the slotted hydrofoil increased by 55% at higher attack angles, with an average performance improvement of 90%. Jin et al. (2021) simulated both breaking and non-breaking conditions of a NACA0024 hydrofoil induced free surface based on experimental data from Mossa (2008) using OpenFOAM. They analyzed the velocity distribution and turbulence intensity of different profiles under both conditions, highlighting that the breaking wave region dissipates approximately 12% of the energy. For this problem, although some three-dimensional effects are included, the above studies show that two-dimensional is sufficient to reflect most physical mechanisms. Building upon previous research, this paper aims to investigate the flow field around NACA0012 hydrofoils at different water depths, the mechanism of air entrainment, and the spatio-temporal distribution of bubbles.

The structure of this paper is as follows: firstly, we will introduce the numerical methods and computational settings, and analyze the sensitivity of the grid. Then, we will investigate the deformation of the free surface under six different water depth conditions: $h/c = 0.3, 0.5, 0.7, 0.9, 1.1$ and 1.3. Combining with vorticity fields, we will explain the variation characteristics of lift and drag coefficients of the hydrofoil. Subsequently, we will conduct a quantitative study on the localized energy dissipation in regions with pronounced wave breaking for three conditions ($h/c = 0.3$, 0.5 and 0.7). Finally, we will focus on categorizing the air entrainment induced by shallowly submerged hydrofoils and study the spatio-temporal characteristics of the large number of bubbles generated after entrainment.

2. Numerical method and computational setup

2.1. Governing equations

This paper is based on the open-source software Basilisk flow solver (Popinet et al., 2018) for incompressible multiphase flow, which is a development of Gerris (Popinet et al., 2009). This software has been validated in various physical phenomena such as wave breaking (Liu et al., 2023), liquid jet atomization (Hashemi et al., 2023), droplet impact dynamics (Sykes et al., 2023), etc. For the air-water two-phase flow problem, its governing equation is as follows:

$$\rho(\partial_t \mathbf{u} + (\mathbf{u}\cdot\nabla)\mathbf{u}) = -\nabla p + \nabla\cdot(2\mu\mathbf{D}) + \mathbf{a} \tag{1}$$

$$\nabla \cdot \mathbf{u} = 0 \tag{2}$$

where $\mathbf{u}$ represents the velocity of the fluid, ρ is the density of the fluid, p denotes the pressure, μ is the dynamic viscosity, $\mathbf{D}$ is the deformation coefficient, defined as $D_{ij} \equiv \left(\partial_i u_j + \partial_j u_i\right)/2$. $\mathbf{a} = \rho \mathbf{g} + \mathbf{F}_\sigma$ represents the gravity and surface tension source terms.

By employing the classical time-splitting projection method, Eqs. (1) and (2) can be discretized in second order:

$$\rho_{n+\frac{1}{2}}\left[\frac{\mathbf{u}_\star - \mathbf{u}_n}{\Delta t} + \mathbf{u}_{n+\frac{1}{2}} \cdot \nabla \mathbf{u}_{n+\frac{1}{2}}\right] = \nabla \cdot \left[\mu_{n+\frac{1}{2}}(\mathbf{D}_n + \mathbf{D}_\star)\right] + \mathbf{a}_{n+1} \tag{3}$$

$$\mathbf{u}_{n+1} = \mathbf{u}_\star - \frac{\Delta t}{\rho_{n+\frac{1}{2}}} \nabla p_{n+\frac{1}{2}} \tag{4}$$

$$\nabla \cdot \mathbf{u}_{n+1} = 0 \tag{5}$$

where the index n denotes the time step. In Eq. (3), the advection term $\mathbf{u}_{n+\frac{1}{2}} \cdot \nabla \mathbf{u}_{n+\frac{1}{2}}$ is discretized using second-order upwind Bell-Collela-Glaz scheme, while the diffusionc term is discretized using second-order Crank-Nicholson scheme. Eq. (5) is combined with Eq. (4) to obtain the pressure-velocity Poisson equation, which is solved using a quad/octree-based multilevel solver.

$$\nabla \cdot \left[\frac{\Delta t}{\rho_{n+\frac{1}{2}}} \nabla p_{n+\frac{1}{2}}\right] = \nabla \cdot \mathbf{u}_\star \tag{6}$$

To solve the intermediate velocity $\mathbf{u}_\star$ in Eq. (3), $\mathbf{u}_{n+\frac{1}{2}}$ is obtained by characteristic extrapolation. Then, according to Eq. (6), the pressure $p_{n+\frac{1}{2}}$ is determined, and $p_{n+\frac{1}{2}}$ is substituted into Eq. (4) to obtain the velocity $\mathbf{u}_{n+1}$ at the next time step.

2.2. Free surface capturing

To capture the free surface, this study employs the Piecewise Linear Interface Calculation (PLIC) method based on the Volume of Fluid (VOF) approach. The fluid volume fraction f is obtained by solving the following transport equation:

$$\partial_t f + \nabla \cdot (f\mathbf{u}) = 0 \tag{7}$$

In this method, the surface tension force is calculated using the formula:

$$\mathbf{F}_\sigma = \sigma \kappa(f) \delta_s \mathbf{n} \tag{8}$$

where σ is the surface tension coefficient, δ_s is the Dirac function of the interface indicating that the surface tension term acts on the interface, and $\mathbf{n}$ is the interface normal. The curvature of the free surface κ, is commonly computed using the following formula:

$$\kappa(f) = -\nabla\left(\frac{\nabla f}{|\nabla f|}\right) \tag{9}$$

However, the derivative of the volume fraction f is not continuous at the free surface, leading to inaccuracies in curvature computation, especially in scenarios involving severe free surface breakup and air entrainment. To address this, the level set method is employed to compute the surface tension:

$$\mathbf{F}_\sigma = \sigma \kappa(\phi) \delta_s \mathbf{n} \tag{10}$$

where ϕ is a continuous distance function.

Therefore, it is also necessary to solve the transport equation of the level set function ϕ:

$$\partial_t \phi + \nabla \cdot (\phi \mathbf{u}) = 0 \tag{11}$$

$$\begin{cases} \phi < 0 & \text{Air phase} \\ \phi = 0 & \text{Free surface} \\ \phi > 0 & \text{Liquid phase} \end{cases} \tag{12}$$

The above method is known as the Coupled Level Set and Volume of Fluid (CLSVOF) method (Limare et al., 2023). It combines the mass conservation capabilities of the geometric reconstruction PLIC-VOF method with the accurate curvature calculations of the Level Set method. The coupling mechanism of these two methods in this study is depicted in Fig. 1 below.

Additionally, to better capture air entrainment and bubble sweep-down, the Adaptive Mesh Refinement (AMR) approach is covered. The AMR adaptively refines and coarsens the grid depending on the refinement criterion using a quadtree/octree mesh structure. The refinement criterion is based on the wavelet algorithm, which estimates numerical errors in the representation of spatially discretized fields. The wavelet algorithm refines or coarsens the mesh by analyzing the local error estimates in the flow field. This method ensures that the computational resources are focused on areas with significant physical changes, thereby capturing the detailed dynamics of bubble and free surface deformation efficiently. More details on the adaptive wavelet algorithm can be found in Popinet (2015). In this study, the maximum tolerance of the estimated error in the velocity field is denoted as $u_{err} = 2 \times 10^{-3}$, and in the volume fraction is set as $f_{err} = 1 \times 10^{-18}$.

By using these advanced techniques, this investigation aims to provide a detailed understanding of the flow dynamics and air entrainment mechanisms around shallowly submerged hydrofoils at different submergence depths.

2.3. Physical model

The schematic diagram of the two-dimensional computational domain for this study is depicted in Fig. 2. The hydrofoil is modeled as a NACA0012 profile with a five-degree angle of attack using the Cartesian cut-cell method (Schwartz et al., 2006). The chord length of the hydrofoil is denoted as c, with the origin of the coordinate system located

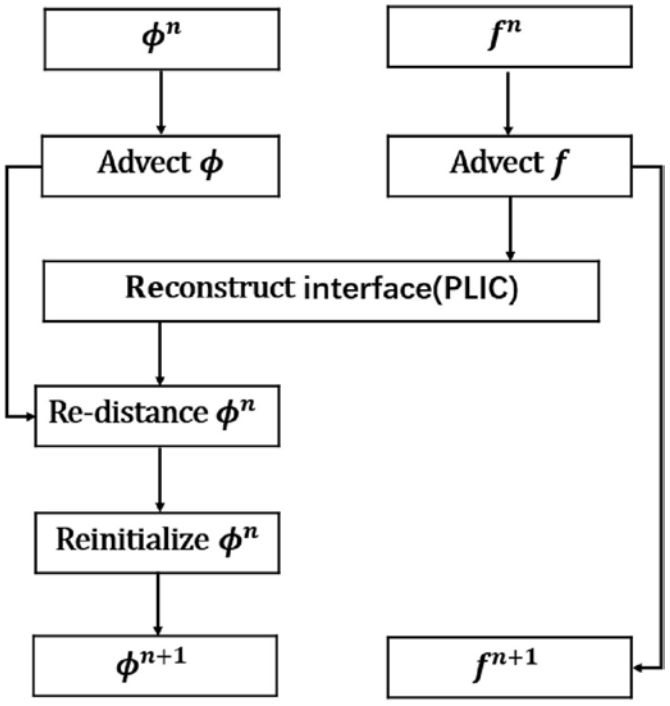

Fig. 1. Flow chart of the CLSVOF Method.

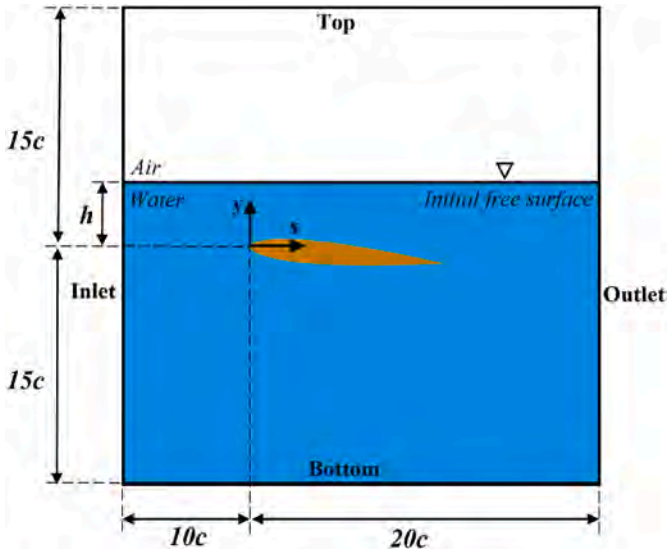

Fig. 2. Physical model and related geometric parameters at the initial time.

at the leading edge of the hydrofoil. The entire computational domain is a square with a side length of 30c, and h represents the submergence depth. The top boundary is positioned at a distance of 15c from the hydrofoil and is set as an atmospheric boundary condition. Similarly, the bottom boundary is also located 15c away from the hydrofoil and set as a no-slip wall. The inlet boundary is positioned 10c away from the hydrofoil to mitigate the influence of inflow and is configured as a Dirichlet velocity boundary. To ensure the full development of the wake, the outlet is positioned 19c away from the trailing edge of the hydrofoil and is configured with Neumann conditions.

To facilitate a better understanding of the mechanisms involved, we employ several dimensionless parameters: The chord-based Froude number is given by $F_{nc} = U/\sqrt{gc}$, and the Reynolds number is $Re_{nc} = \rho Uc/\mu$, where μ is the dynamic viscosity of water. The submergence depth is expressed as h/c, and the dimensionless computation time is $t^* = tU/c$, with t representing the computation time. The hydrofoil's lift coefficient is calculated as $C_L = F_L/\left(\frac{1}{2}\rho U^2 c\right)$, and the drag coefficient is $C_D = F_D/\left(\frac{1}{2}\rho U^2 c\right)$, where F_L and F_D are the computed lift and drag forces, respectively, and ρ is the density of water.

In this study, the chord length c of the hydrofoil is 1 m, and the inflow velocity is set to $U = 1.789$ m/s, corresponding to $F_{nc} = U/\sqrt{gc} = 0.571$ and $Re_{nc} = 1.569 \times 10^6$. The specific submergence depth ratio and the immersion-based Froude number are presented in Table 1. The density ratio between air and water is 1/998, with the dynamic viscosity ratio of $1.784 \times 10^{-5}/1.138 \times 10^{-3}$. The gravitational acceleration is set to $g = 9.81$ m/s^2, and the surface tension coefficient is 0.07 N/m.

2.4. Code verification and grid sensitivity analysis

In this section, we first validate the applicability of the current numerical method to the problem. The operating conditions are set according to Duncan (1983), with $h/c = 1.03$ and $c = 0.2\ m$ ($U = 0.8$ m/s; $F_{nc} = 0.571$). We extract the wave height behind the hydrofoil and compare our results with experimental data and the numerical results of Pernod et al. (2023) as shown in Fig. 3. We observe that our results exhibit good phase agreement with the experimental results. However, our results show slightly smaller wave heights compared to the experimental data. This discrepancy is attributed to the relatively distant bottom boundary set in our study, which corresponds to deep-water conditions. In contrast, the experimental setup involves a limited water tank height, leading to a shoaling effect. This slight underestimation of wave peaks is also observed in the studies of other researchers (Ali and Karim, 2010; Prasad et al., 2015).

Table 1
Simulation conditions.

Condition	h/c	F_{nh}
1	0.3	1.04
2	0.5	0.81
3	0.7	0.68
4	0.9	0.60
5	1.1	0.54
6	1.3	0.50

Since the experimental setup did not measure the forces acting on the hydrofoil, we compare the lift and drag coefficients of the hydrofoil with numerical results from other studies (Prasad et al., 2015; Pernod et al., 2023), as summarized in Table 2. For the lift coefficient C_L, our study yields a result of 0.6081, with an error of −4.19% compared to Prasad and −0.75% compared to Pernod. Regarding the drag coefficient C_D, our study results in 0.0313, falling between the numerical results of the other two studies, with an error of −11.8% compared to Prasad and 18.11% compared to Pernod. Overall, considering the deformation of the wave surface and the forces acting on the hydrofoil, our numerical method aligns well with experimental data and numerical results from other studies, demonstrating its applicability to the problem.

To investigate the phenomenon of air entrainment more effectively, this study sets the chord length of the hydrofoil as $c = 1\ m$. Three maximum levels of grid refinement $l_{max} = 11(\Delta_{min} = c/68)$, $l_{max} = 12(\Delta_{min} = c/136)$ and $l_{max} = 13(\Delta_{min} = c/272)$ are employed to study grid sensitivity, with the total computational time $t^* = 170$. For the condition with the lowest degree of free surface deformation $h/c = 1.3$, the time-averaged free surface is shown in Fig. 4. From the figure, we observe that the shapes of the free surface are generally similar among the three refinement levels, except for slight differences in the trough of the leading wave on the coarsest grid.

For the most intense free surface breaking condition $h/c = 0.3$, Fig. 5 illustrates the instantaneous free surface at times $t^* = 3.0$ and $t^* = 3.1$, corresponding to the moment of initial roll-up and breaking of the free surface. It can be seen from the figure that the roll-up of the free surface is well captured at all three refinement levels.

It is evident from the above that under the three maximum refinement levels, the numerical results in the grid do not significantly change. To better capture the air entrainment and the bubble dynamics in the flow field, the study is conducted using $l_{max} = 12$. Fig. 6 depicts a schematic of adaptive grid refinement. It can be observed that the adaptive strategy effectively enhances grid resolution, particularly in regions such as the free surface and the wake vortex shedding area of the hydrofoil.

3. Results and discussions

3.1. Free surface deformation

Fig. 7 depicts the instantaneous volume fraction contours for the different conditions. From the figure, it is clear that the free surface undergoes significant deformation for $h/c = 0.3$、0.7 and 0.9. In contrast, for $h/c = 1.1$ and $h/c = 1.3$, the interface shows minimal deformation, presenting regular wave-like patterns. Furthermore, wave profiles extracted at this moment are illustrated in Fig. 8. From this figure, the deformation of the wave surface is more pronounced. In the range $h/c = 0.3$ to $h/c = 0.9$, as the depth increases, the degree of wave breaking gradually decreases, while the wave height increases, and the wave profiles become more complete. However, for $h/c = 1.1$ and $h/c = 1.3$, relatively intact wave shapes are observed. Notably, the wave height and steepness for $h/c = 1.3$ appear smaller than those for $h/c = 1.1$. This is attributed to the diminishing influence of the hydrofoil

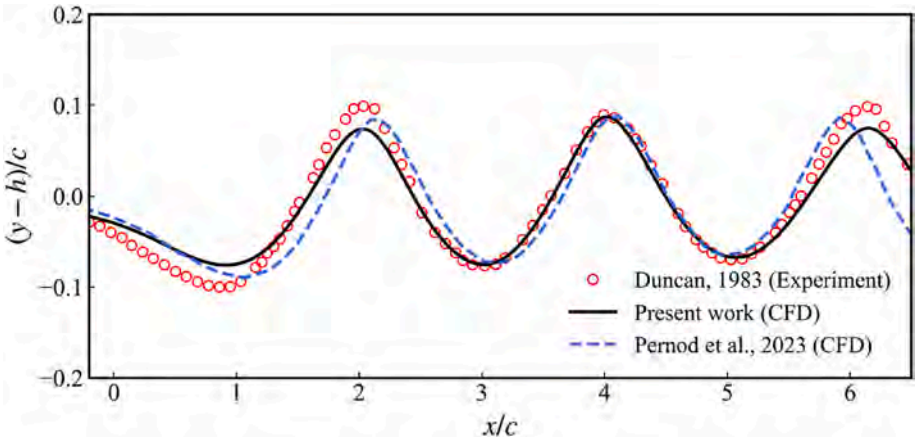

Fig. 3. Comparison of free surface deformation.

Table 2
Results of lift and drag coefficients.

Results	C_L	C_D
Present work	0.6081	0.0313
Prasad et al. (2015)	0.6347	0.0355
Error	−4.19%	−11.8%
Pernod et al. (2023)	0.6127	0.0265
Error	−0.75%	18.11%

disturbance on the free surface as the hydrofoil moves farther away from it.

For the three conditions with serious free surface deformation, $h/c = 0.3, 0.5$ and 0.7, we conducted a time average of the volume fraction field from $t^* = 70$ to $t^* = 170$, as shown in Fig. 9. In the condition of $h/c = 0.3$, the breaking zone of the leading wave is most pronounced and extensive. Additionally, we observe that the entrapped bubbles sweep downstream after wave breaking. As for the $h/c = 0.5$ and 0.7 conditions, the peaks of the leading wave are higher, and more complete. Furthermore, the distribution range and sweep-down depth of the

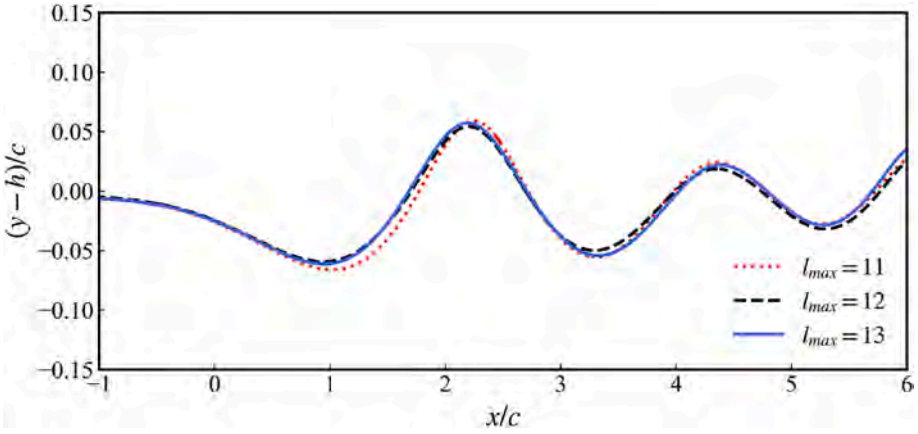

Fig. 4. Time-averaged free surface deformation under three refinement levels at $h/c = 1.3$.

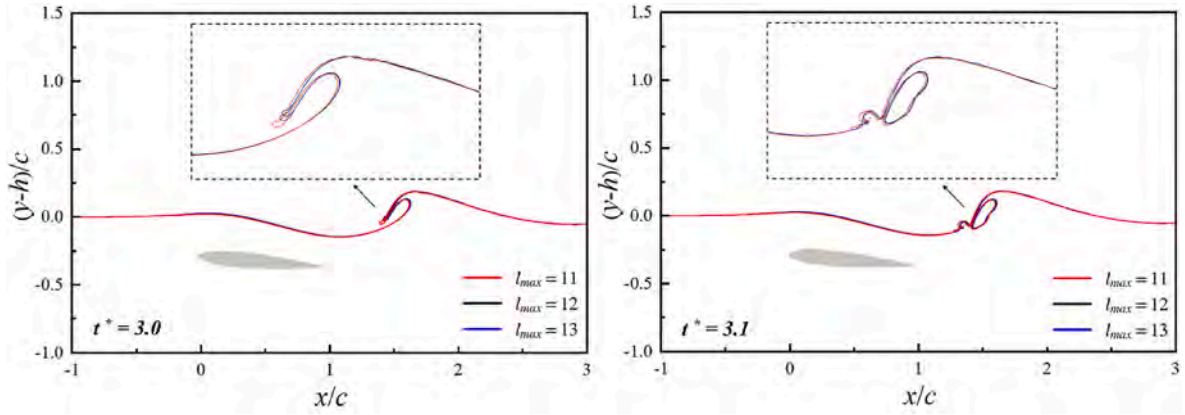

Fig. 5. Instantaneous free surface deformation under three refinement levels at $h/c = 0.3$.

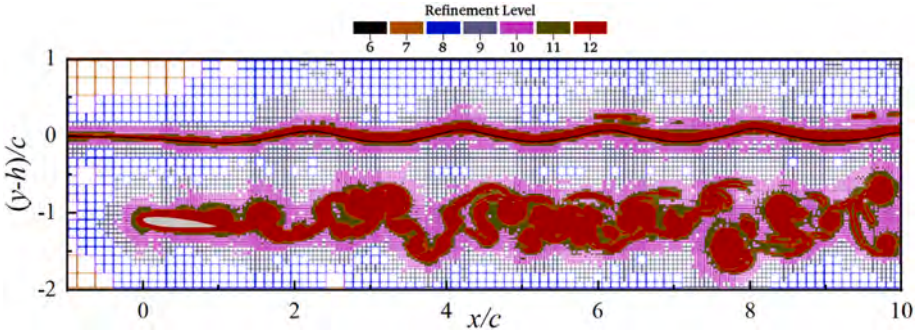

Fig. 6. Grid adaptive refinement diagram.

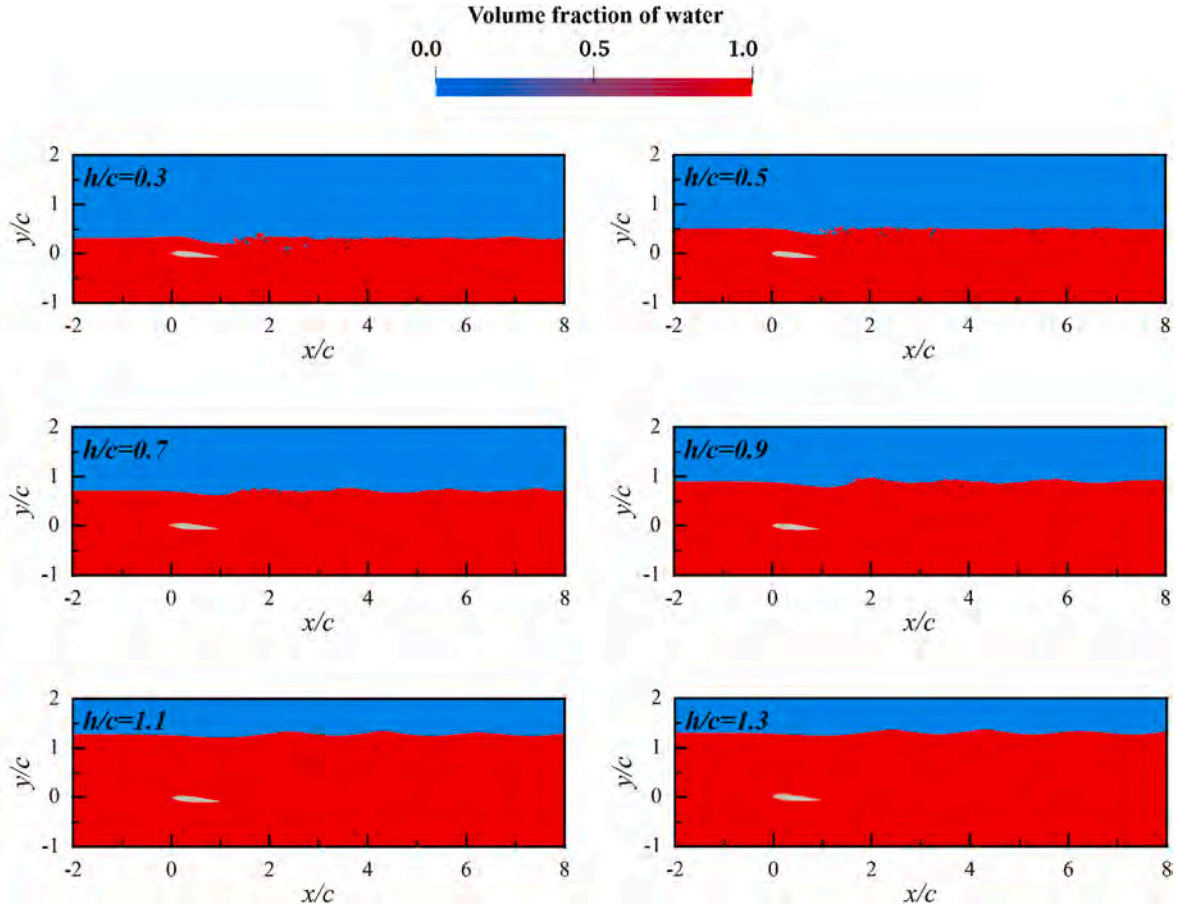

Fig. 7. Contour of water volume fraction at $t^* = 170$.

bubbles are smaller compared to the $h/c = 0.3$ condition.

To further investigate the flow field around the hydrofoil, Fig. 10 illustrates the vorticity in the wake of the hydrofoil. It is observed that the vorticity in the wake of the hydrofoil alternates between positive and negative vortices. On one hand, as the hydrofoil approaches the free surface, these vortices become more tightly packed along the streamwise direction, coinciding with pronounced deformation of the free surface. Significant energy dissipation is indicated by the chaotic distribution of vortices in this area, which disappear as the fluid travels upward into the air region and downstream into the wake zone. On the other hand, as the hydrofoil moves away from the free surface, the vortices gradually spread outwards, with the distribution range increasing and the frequency of alternation between positive and negative vortices decreasing. Observing the free surface, we note a decrease in the presence of vortices near the free surface, and the free surface itself does not exhibit marked fragmentation.

We extracted the lift and drag coefficients of the hydrofoil under these six conditions, as shown in Fig. 11. Although there are no corresponding experimental data for comparison, the trend is quite similar to those obtained by other scholars in previous studies (Ali and Karim, 2010; Prasad et al., 2015; Pernod et al., 2023). The lift and drag coefficients gradually approach the value of the infinite water depth condition as the hydrofoil moves away from the free surface. It is noticeable that with an increase in submersion depth, the lift coefficient of the hydrofoil gradually grows, exhibiting a wide range of variation. Moreover, for the conditions with $h/c = 0.9, 1.1$ and 1.3, the lift coefficients are relatively close, around 0.54. This suggests that the distance between the hydrofoil and the free surface significantly influences the lift coefficient, particularly the impact of wave breaking phenomena on the pressure field of the upper part of the hydrofoil. For h/c greater

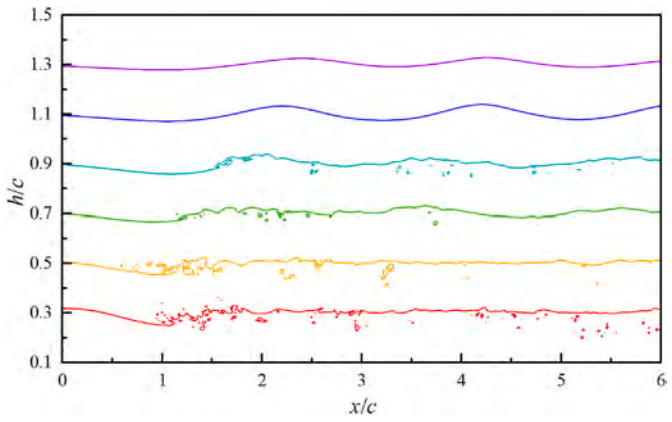

Fig. 8. Comparison of wave profiles at $t^* = 170$.

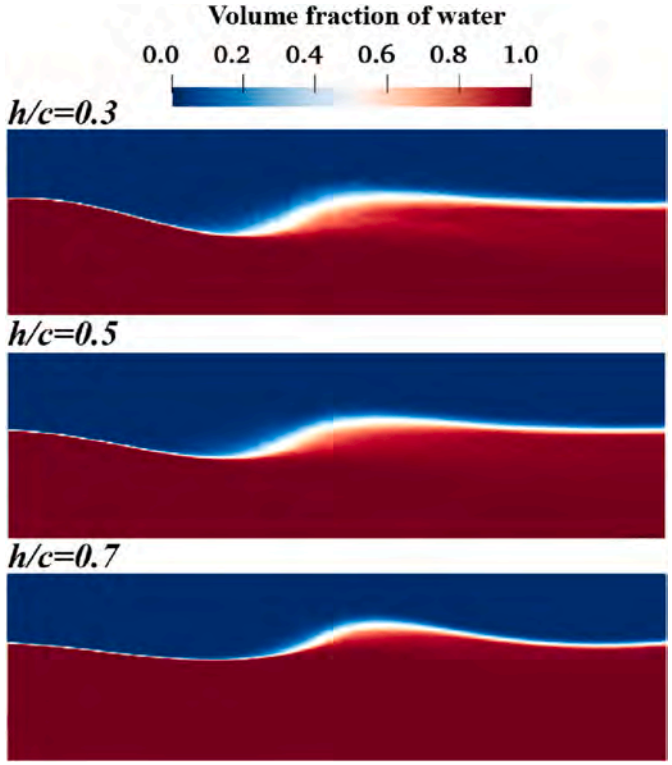

Fig. 9. Time-averaged contour of water volume fraction.

than 0.9, the pressure field around the hydrofoil is approaching conditions like to those in deep water. Additionally, as the submersion depth increases, the drag coefficient gradually decreases, with the drag coefficients for conditions $h/c = 0.7, 0.9, 1.1$ and 1.3 being close, around 0.038. This means that the drag coefficient of the hydrofoil includes wave breaking resistance, and when the free surface deformation is more severe, the drag coefficient of the hydrofoil also increases accordingly. Table 3 presents the standard errors of the lift and drag coefficients, respectively. From the table, it can be seen that as h/c decreases, the more severe the free surface breaking, the more unstable the flow field around the hydrofoil becomes, leading to higher standard errors in the lift and drag coefficients. This phenomenon is similar to the findings of Prasad et al. (2015). Particularly for the condition $h/c = 0.3$, due to the breaking of the free surface, the instability of the flow field around this condition is the strongest.

3.2. Energy dissipation process

In this section, we first compute the distribution of turbulent kinetic energy (TKE) around the hydrofoil, as shown in Fig. 12. The extreme values of turbulent kinetic energy are mainly distributed in the leading wave region where wave breaking occurs. In this region, large-scale coherent structures and shear-induced collapse of air cavities and bubbles enhance the turbulence intensity. In the downstream region, areas with higher turbulent kinetic energy are mainly associated with the free surface. As the vortex motion weakens and larger air bubbles rise and escape to the free surface while smaller bubbles disperse, the extreme values of turbulent kinetic energy rapidly decrease. When the submergence depth is small, the more pronounced shear flow generated by severe wave breaking enhances turbulence mixing and flow pulsation intensity. Additionally, we observe a region of significantly higher turbulent kinetic energy behind the hydrofoil for all three conditions. Furthermore, the distribution range and extreme values of turbulent kinetic energy behind the hydrofoil also rise with increasing submergence depth. This is because, as Fig. 10 illustrates, when the hydrofoil is far from the free surface, the free surface has little effect on the vortex formations, resulting in larger velocity fluctuations in the wake flow field. Furthermore, the zone of extreme turbulent kinetic energy at the hydrofoil's tail gradually approaches the free surface for small submergence depths, whereupon it merges with the region of extreme turbulent kinetic energy near the free surface. However, this phenomenon does not occur for larger submergence depths, indicating that the free surface affects the range of velocity fluctuations and energy dissipation of the hydrofoil wake.

The definitions of fluctuating velocity $\mathbf{u}'$ and turbulent kinetic energy k are as follows:

$$\mathbf{u}' = \mathbf{u} - \overline{\mathbf{u}} \tag{13}$$

$$k = \frac{1}{2}\overline{\mathbf{u}'\mathbf{u}'} \tag{14}$$

$$k^* = \int_{h-c}^{h} k dy \tag{15}$$

The turbulent kinetic energy is vertically integrated to obtain the one-dimensional distribution of turbulent kinetic energy k^* along the streamwise direction, as shown in Fig. 13, where $k^*_{0.3}$ represents the maximum value for the $h/c = 0.3$ condition. The curve of turbulent kinetic energy exhibits a prominent peak along the streamwise distribution, approximately located near $x/c = 1.5$, corresponding to the area of leading wave breaking. The maximum value of $h/c = 0.5$ at this location is 90% of $h/c = 0.3$, while for $h/c = 0.7$, it is only 60% of $h/c = 0.3$. This indicates that the degree of free surface disruption induced by the hydrofoil significantly affects the distribution of turbulent kinetic energy in the flow field. In general, the three curves exhibit an upward trend, a downward trend, and finally converge to equivalent turbulent kinetic energy values at $x/c = 6$. This suggests that in conditions where wave breaking is more severe, turbulent kinetic energy dissipation occurs more quickly, but it eventually stabilizes in the downstream far-field. The turbulent kinetic energy curve of the $h/c = 0.7$ condition shows two peaks of comparable magnitude following the first peak, which corresponds to the peak region of the wave profile in the flow field. This is owing to the turbulent kinetic energy curve is influenced by wave height in this region, with strong turbulence zones near the free surface.

Fig. 14 displays the time-averaged velocity field and pressure field around the hydrofoil. The pressure represents dynamic pressure. From the figure, it is shown that the pressure on the air side can be neglected, while the pressure on the water side has a significant impact. For the $h/c = 0.3$ condition, due to the blockage effect between the hydrofoil and the free surface, the flow velocity in the upper region of the hydrofoil increases, forming a low-pressure area at the trailing edge of the

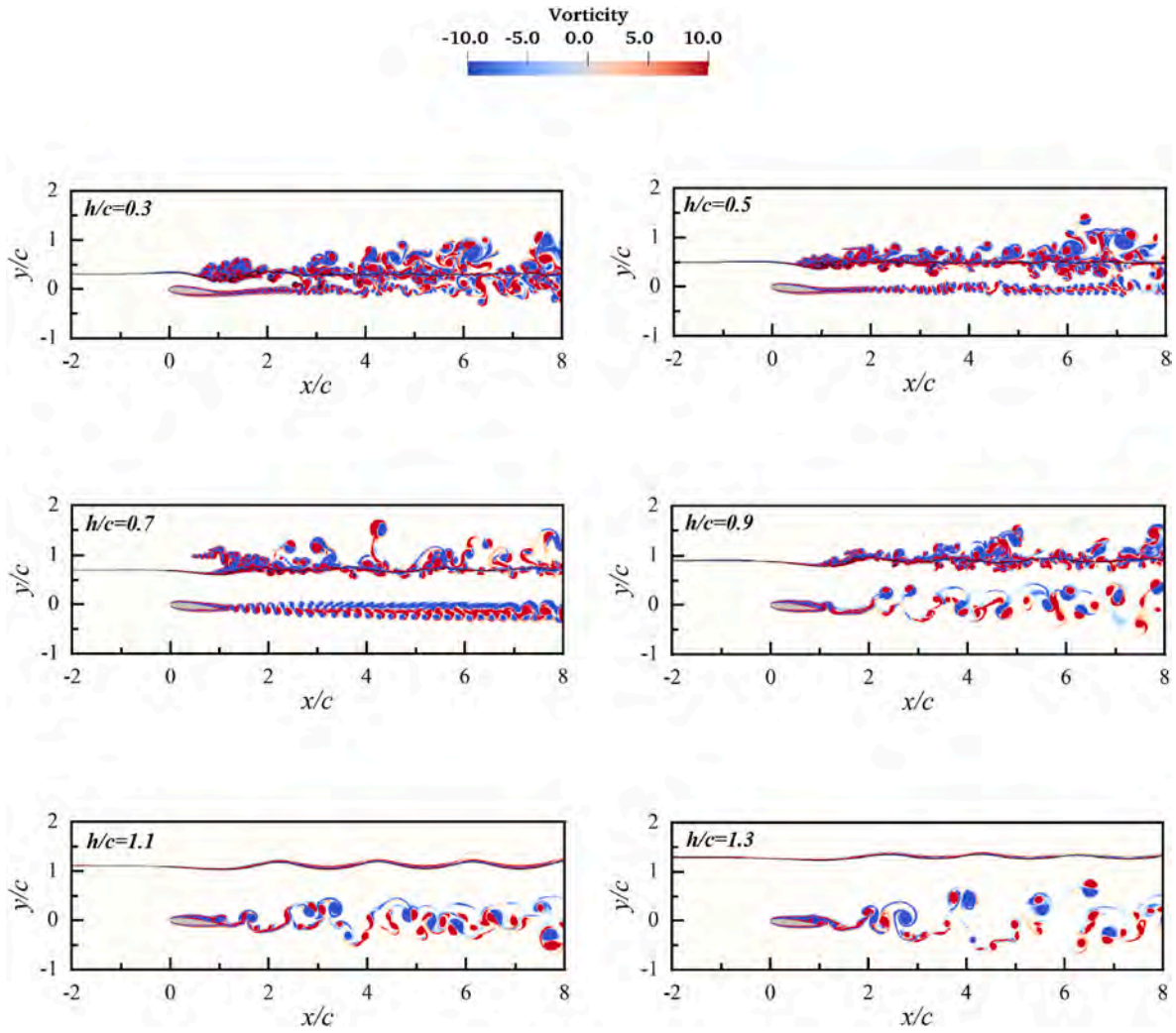

Fig. 10. The vorticity contour diagram and free surface deformation at $t^* = 170$.

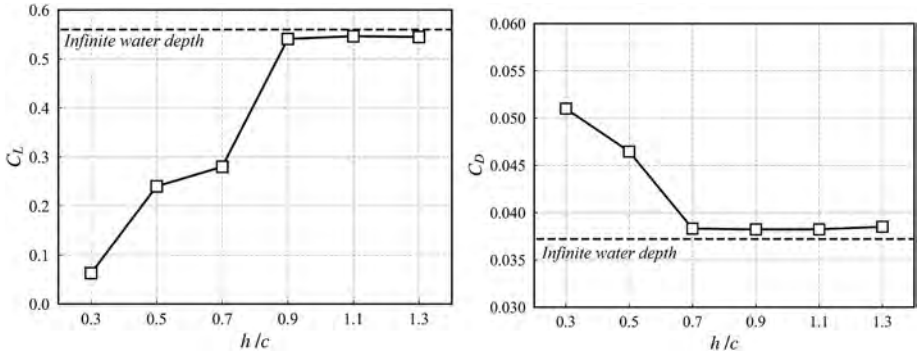

Fig. 11. Lift coefficient and drag coefficient of hydrofoil.

Table 3
Error of lift and drag coefficients.

h/c	0.3	0.5	0.7	0.9	1.1	1.3
C_L	0.06288	0.241	0.280	0.0544	0.5464	0.5448
Standard Error	7.63%	5.14%	4.86%	3.17%	1.38%	0.74%
C_D	0.0511	0.0465	0.0383	0.0382	0.0382	0.0386
Standard Error	8.27%	7.20%	5.11%	3.43%	2.74%	2.18%

hydrofoil. This low-pressure area connects the upper surface of the hydrofoil and the free surface. As the submergence depth increases, the range of the low-pressure area expands and moves toward the leading edge of the hydrofoil, eventually forming a low-pressure area at the front part of the hydrofoil. The continuously breaking free surface near the hydrofoil disrupts the low-pressure area on its upper surface, and results in a reduced lift coefficient. This explains the increase in the lift coefficient of the hydrofoil with increasing submergence depth in Fig. 11. For the $h/c = 0.7$ condition, due to less wave breaking influence, the

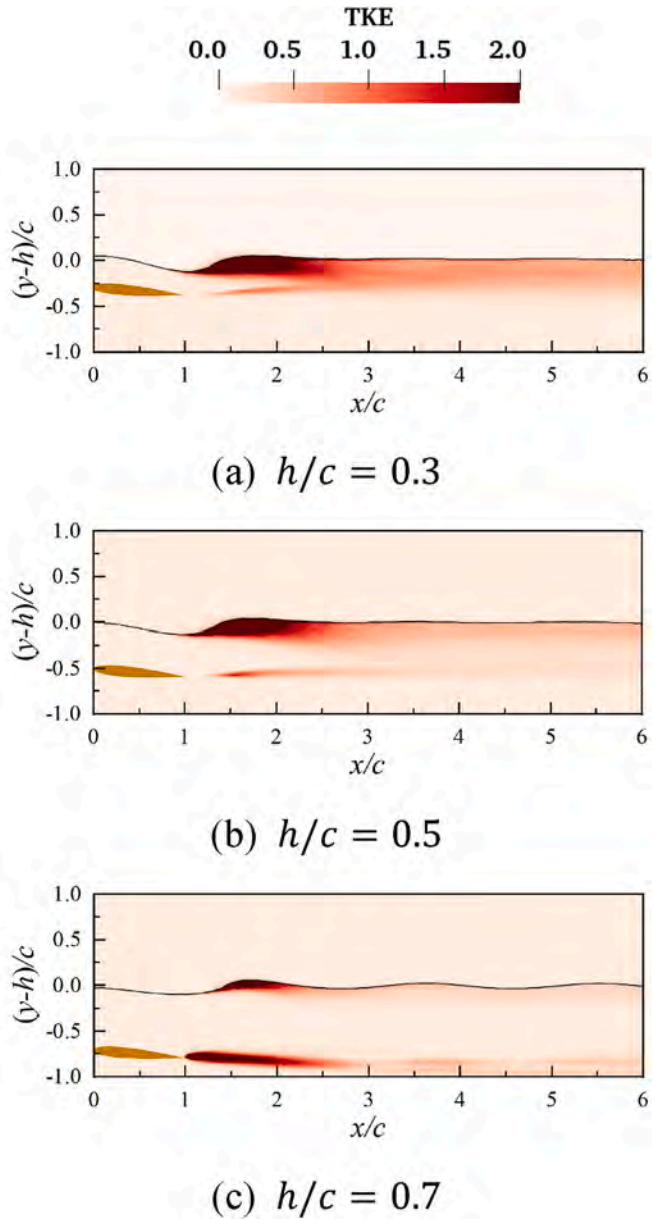

Fig. 12. Turbulent kinetic energy distribution.

wave profile is relatively intact, and the pressure alternates between positive and negative at the wave peaks and troughs. Regarding the velocity field, the velocity on the air side remains at the inflow velocity and decreases near the free surface. The existence of a region with lower velocity in the leading wave breaking area, where the wave breaks against the incoming flow, is a prominent feature for all three situations. The smaller the submergence depth of the hydrofoil, the stronger the interaction between the hydrofoil and the free surface, leading to higher flow velocities in this region and an increased drag coefficient of the hydrofoil. In practical conditions, the sailing hydrofoil provides energy for the continuous breaking of the free surface, resulting in an increase in wave-breaking resistance as a component of the total resistance. In addition, due to vortex structures, two separate velocity bands with a discernible velocity difference between them can be seen in the hydrofoil's wake.

To evaluate energy dissipation, it is useful to compute the decay of the energy equation by integrating it along streamwise direction. With this approach, all factors influencing energy dissipation can be considered. The energy balance equation can be used to determine the total

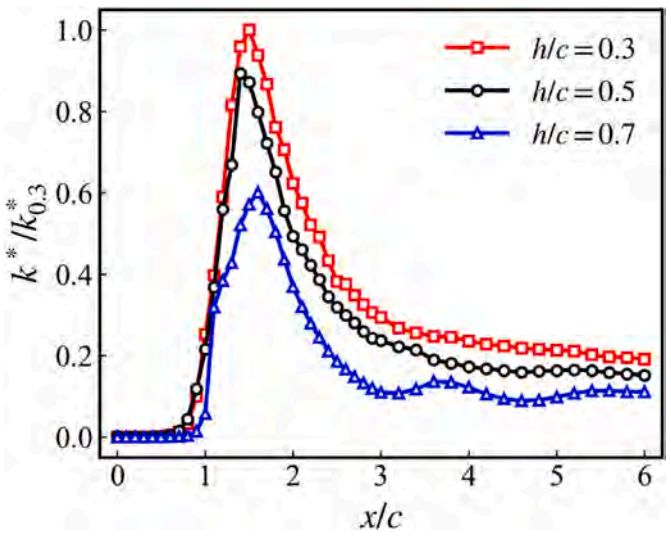

Fig. 13. One dimensional distribution of turbulent kinetic energy along streamwise direction.

fluid energy dissipation ratio, based on the time-averaged energy flow deficit. The measured mean kinetic flux F_k per unit area and mean potential flux F_p,is defined as:

$$F_k = \overline{\int_{h-c}^{h} \left[\frac{1}{2}\rho(u^2+v^2)\right] u dy} \tag{16}$$

$$F_p = \overline{\int_{h-c}^{h} [P+\rho g y] u dy} \tag{17}$$

Where, h represents the position of the free surface. Therefore, for the total energy flux

F, it is given by:

$$F = F_k + F_p = \overline{\int_{h-c}^{h} \left[P + \frac{1}{2}\rho(u^2+v^2) + \rho g y\right] u dy} \tag{18}$$

The energy dissipation ratio D_F is defined as:

$$D_F = \left(F_{x/c} - F_0\right) / F_0 \tag{19}$$

In this equation, $F_{x/c}$ represents the local energy flux at the position x/c, and F_0 denotes the energy flux at $x/c = 0$.

The flow field can be divided into four sections in the streamwise direction: the steady zone ($x/c \leq 0$), the wave breaking zone ($0 < x/c \leq 1$), the dissipation zone ($1 < x/c \leq 2$), and the quasi-steady zone ($x/c > 2$).

In the steady zone, as depicted in Fig. 15, the free surface is unaffected by the hydrofoil and remains undistorted, maintaining stable kinetic and potential energy. At $x/c = 0$, for the conditions with $h/c = 0.3, 0.5$ and 0.7, the potential energy flux accounts for 77%, 75%, and 72%, respectively, while the kinetic energy flux accounts for 23%, 25%, and 28%. The distribution of these energy components is relatively uniform, with variations only due to the hydrofoil's submergence depth.

In the wave breaking zone, as depicted in Fig. 15, the free surface forms a head defect, leading to an initial decrease in potential energy. However, due to the constriction caused by the hydrofoil shape, the volume of water increases, raising the potential energy again. Due to the obstructing effect of hydrofoil, the velocity of water in this area increases, and the kinetic energy flux curve shows a great increase and finally reaches a peak. Energy dissipation initially decreases slightly compared to the $x/c = 0$ position, then increases to a peak in the total energy curve. The tendency of energy reduction becomes less noticeable as the submergence depth rises. Due to the reason that the potential

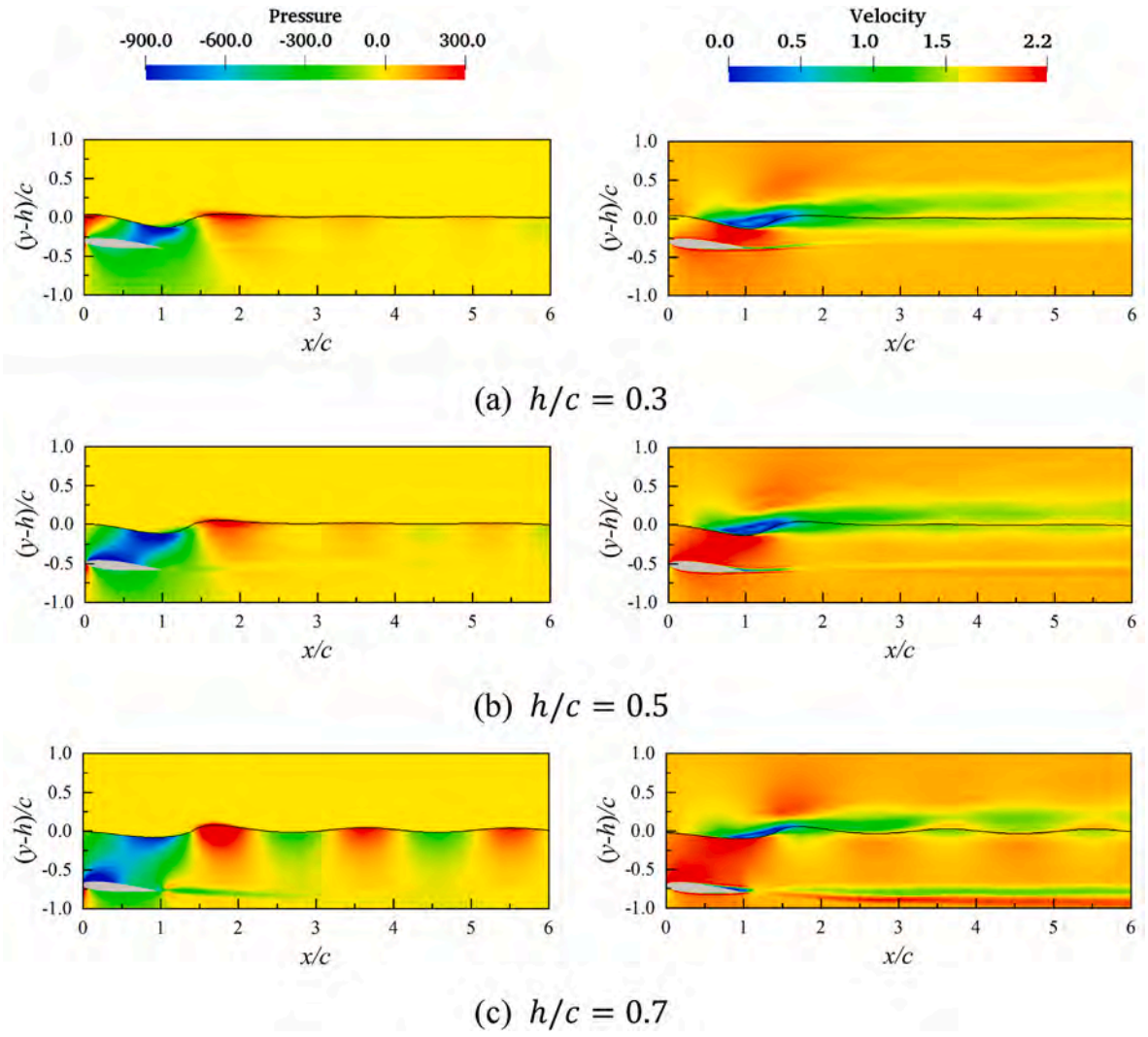

Fig. 14. Time-average pressure distribution and velocity distribution.

energy reduction is slowed and the head defect depth is lessened by the diminished wave breaking intensity. The maximum energy increase for the conditions with $h/c = 0.3, 0.5$ and 0.7 occurs around $x/\ c\ =\ 1$, with increases of 5.35%, 4.21%, and 3.42%, respectively. This additional energy is mainly due to the hydrofoil's disturbance of the free surface, representing an extra energy loss compared to deep water conditions.

In the dissipation zone, as shown in Fig. 15, the region moves progressively away from the hydrofoil and encompasses the widest distribution of turbulent kinetic energy after wave breaking, indicating the most intense turbulence. The total energy drops sharply in this region. At $x/c = 2$, the total energy nearly matches the energy a $x/\ c\ =\ 0$, indicating that the additional energy gained by the water in the previous zone is entirely dissipated here. From the time-averaged free surface in Fig. 14, this region shows the bottom of head defect beginning to rebound, including the first wave crest. Potential energy initially increases and then slightly decreases in this region, following the free surface undulations and increasing compared to $x/c = 0$. The kinetic energy flux continuously decreases in this zone, with the reduced kinetic energy converting into potential energy.

In the quasi-steady zone, as depicted in Fig. 15, the potential energy flux curves for all three conditions show slight undulations but overall remain stable at the same constant value, equivalent to 77.3% of the energy at $x/c = 0$. The kinetic energy flux exhibits a wavy pattern, with greater fluctuations at higher submergence depths. The fluctuation period of the three conditions is close to 1.6c. This behavior is likely caused by vortices in the hydrofoil's wake, and as the vortices expand downstream, the kinetic energy flux in the flow field also increases.

3.3. Entrainment process

In our observations, three distinct types of air entrainment at the free surface are identified, as shown in Fig. 16, which illustrates the vorticity field and free surface deformation at $t^* = 170$. When submergence depth is small, such as $h/c = 0.5$ condition, three different types of air entrainment mechanisms are evident in Fig. 16(a). We designate these three types as Type-I, Type-II, and Type-III. Type-I and Type-III resemble the air entrainment types induced by a rotating cylinder, as reported by Guo et al. (2023). However, the underlying mechanisms are not further analyzed in their study. It is found that with increasing submergence depth, Types I and II gradually disappear, leaving only Type-III, as illustrated in Fig. 16(b) for the $h/c = 1.1$ condition. The mechanisms behind these three types of air entrainment are analyzed in detail below.

Fig. 17 demonstrates air entrainment of Type-I, primarily caused by the leading wave breaking on the free surface. This type encompasses the largest volume of entrained air among all types. In the initial stage of flow ($t^* = 1.34$), the flow velocity between the upper side of the hydrofoil and the free surface increases, creating a low-pressure zone, as shown in Fig. 14. Consequently, the free surface depresses under atmospheric pressure. Around $x/c = 1.7$, the increased flow volume causes the free surface to rise, forming a wave crest. When the wave

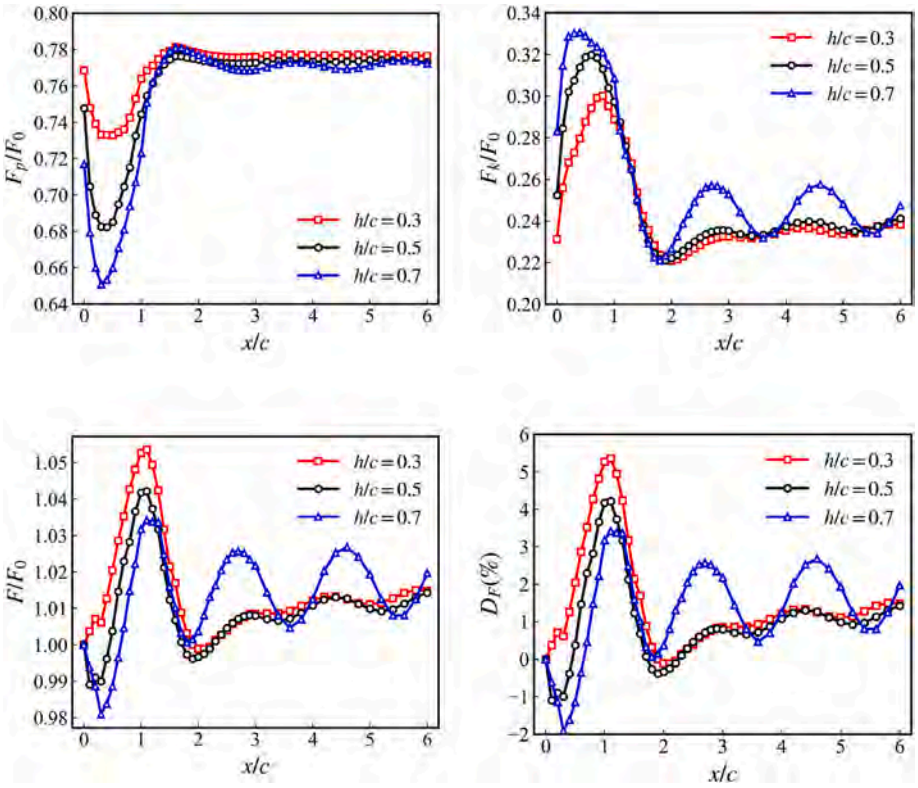

Fig. 15. Variations of the energy flux and total energy dissipation rate along streamwise direction.

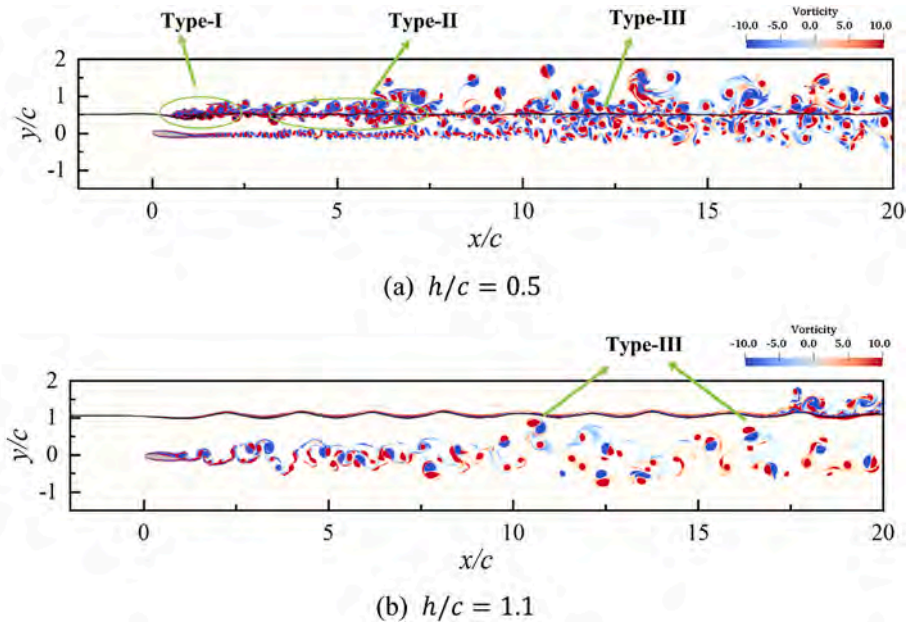

Fig. 16. Three types of bubble entrainment.

steepness exceeds the threshold and driven by the higher velocity at the base, the upper wave surface overturns, creating a water tongue that impacts the upstream water surface ($t^* = 6.26$). Air is entrained as large-scale cavities by the overturning water tongue ($t^* = 6.71$), and the impact creates a second smaller tongue that continues to entrain air upstream. Finally, this area exhibits a turbulent rolling state of water-air mixing, with continuous free surface breaking and air entrainment ($t^* = 170.00$), similar to the phenomenon of hydraulic jumps (Li et al., 2021).

The entrained air forms bubbles of various scales under the shear action of upper and lower layer flows. Some bubbles are carried upstream by large-scale turbulent eddies or rise to escape the surface due to buoyancy. Others are transported downstream within the shear layer, inducing Type-II air entrainment, as shown in Fig. 18. Here, bubbles move downstream in a positive vortex rotation state. When nearing the free surface, the bubbles do not escape directly but cause the free surface to overturn and form jets that break downstream. Few amounts of air are entrained by these jets and travel through the water as negative vortices. These vortices interact with the positive vortex bubbles beneath the free

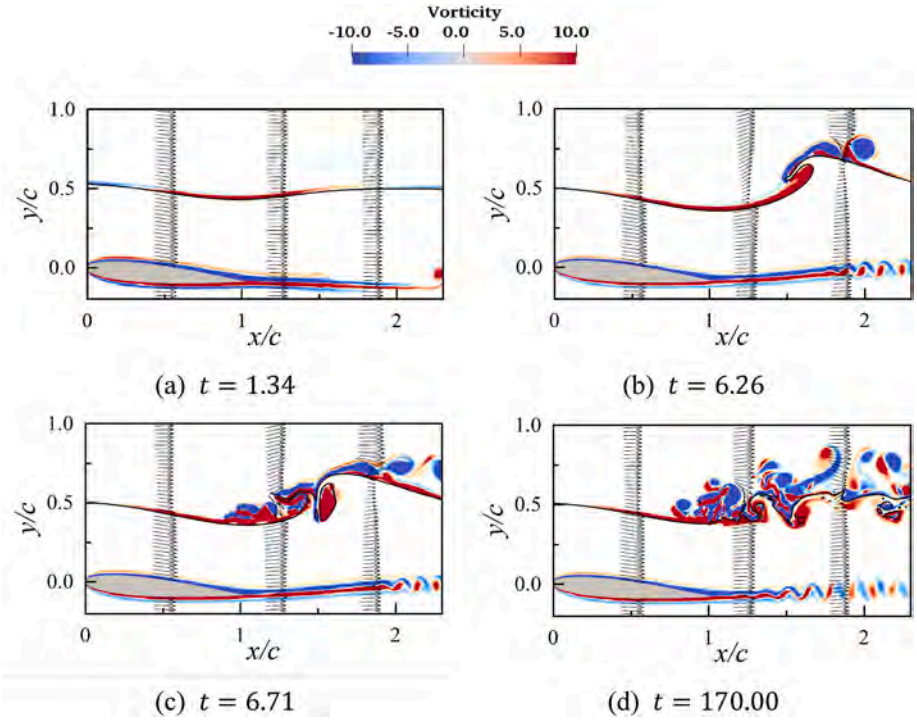

Fig. 17. The bubble entrainment of Type-I

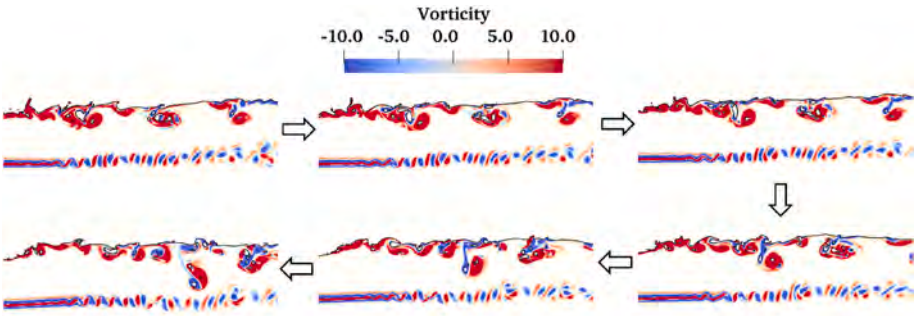

Fig. 18. The bubble entrainment of Type-II

surface, diffusing deeper and breaking into smaller bubbles. This Type-II mechanism explains why high waves do not form downstream.

Fig. 19 shows Type-III bubble entrainment. The hydrofoil creates alternating positive and negative vortices in its wake. As these vortices flow downstream and spread laterally, they interact with the free surface, causing Type-III entrainment. The interaction mechanism is similar to Type-II, but involves vortex pairs instead of a single vortex. When vortex pairs interact with the free surface, depending on the rotation direction of the contacting vortex, the free surface breaks in different directions. As shown in Fig. 19, vortex V1 interacts with the free surface, causing air entrainment, forming bubbles wrapped by vortex V3. Due to vortex V2, V1 and V3 are confined near the free surface, leading to multiple air entrainment events. With multiple breakings, vortices V1 and V2 quickly dissipate, leaving vortex V3 to merge with V2, while V1 wraps around V2. Vortex V3 then dominates, controlling the downstream flow of the vortex cluster. During this process, large bubbles are stretched and split into smaller bubble groups.

3.4. Spatial-temporal characteristics of bubbles

Fig. 20 shows the time curve of the total entrained bubble volume for the $h/c = 0.5$ condition, with time and volume presented in dimensionless units. At $t^* = 7.3$, the first wave overturns at the free surface, forming a large air cavity. This cavity quickly breaks up, and the large bubbles rise to the surface, causing a sharp decrease in bubble content. However, subsequent smaller breaking wave events lead to a repeated increase in bubble volume. Thus, the entire curve exhibits a fluctuating pattern, where the troughs correspond to the escape of large bubbles, and the peaks correspond to steep wave breaking in the leading wave region. For instance, at $t^* = 77.3$, a jet formed in the turbulent flow traps a new air cavity. Despite the repeated fluctuations, the time-averaged total bubble volume remains around 0.021.

From Fig. 20, it can be observed that the total volume of entrained bubbles in the water oscillates around the mean value over time. Consequently, we extracted the time-averaged entrained air volume for six different submergence depths, as shown in Fig. 21. The total volume of entrained air decreased as submergence depth expands, mostly due to the declining significance of Type-I entrainment. This explains why the total air volume for the $h/c = 0.3$ and $h/c = 0.5$ is considerably higher than for other conditions. Additionally, for the $h/c = 1.1$ and $h/c = 1.3$, only Type-III entrainment is present, resulting in a lower total volume of entrained bubbles.

The bubble density spectrum $\overline{N}(r_{\text{eff}})$ is calculated using the effective

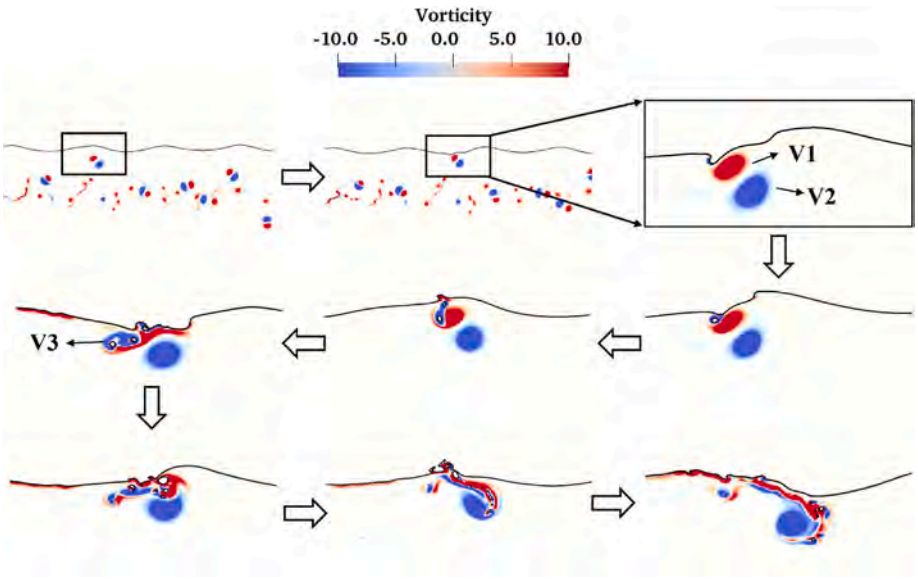

Fig. 19. The bubble entrainment of Type-III

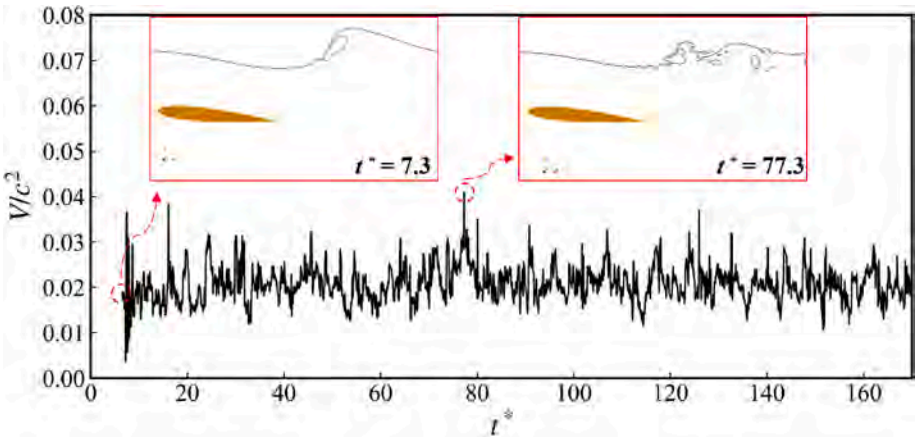

Fig. 20. The curve of the bubble volume over time at $h/c = 0.5$.

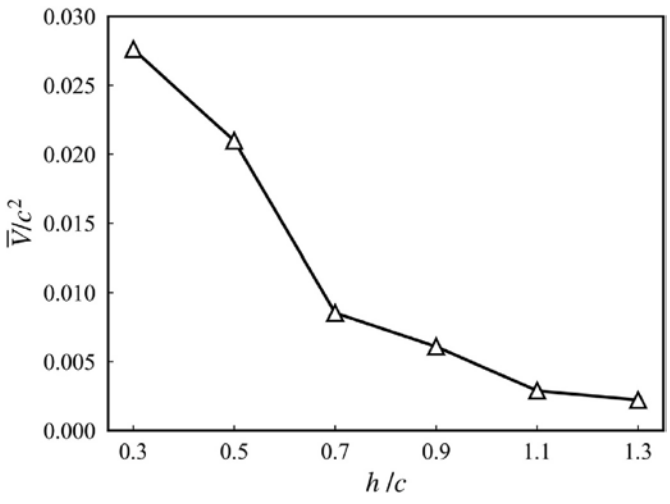

Fig. 21. Time-averaged bubble volume.

radius r_{eff}. The number of bubbles $n(r_{\text{eff}}, b)$ per bin size b is time-averaged over the selected calculation period and the divided by the total volume of entrained bubbles, as shown in the following equation:

$$r_{\text{eff}} = \left(\frac{3v_b}{4\pi}\right)^{\frac{1}{3}} \tag{20}$$

$$\overline{N}(r_{\text{eff}}) = \frac{1}{T}\int_t^{t+T} \frac{n(r_{\text{eff}}, b)}{b} dt \tag{21}$$

$$\overline{N}_0 = \int_0^{r_{max}} \overline{N}(r; b)\frac{4}{3}\pi r^3 dr \tag{22}$$

where b is set to 0.1c, and the time-averaging process is consistent with the previously selected time period, from $t^* = 70$ to $t^* = 170$.

Fig. 22 presents the bubble density spectrum for the six conditions. It can be seen that all conditions follow a power-law distribution with an exponent of $-10/3$, indicating that turbulent shear is the primary mechanism controlling bubble cluster formation. This result is consistent with numerous previous studies (Hendrickson and Yue, 2019; 2022). Additionally, it is found that as the submergence depth increases, the number of large bubbles decreases, indicating that Type-I air entrainment is the main source of large bubbles. Furthermore, as bubble

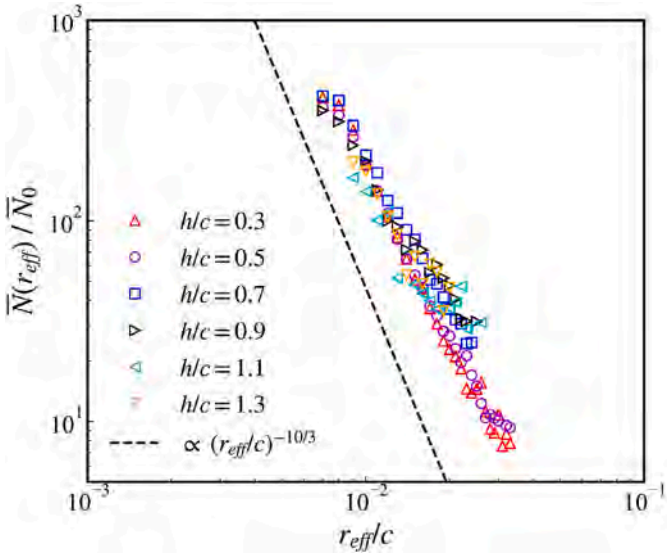

Fig. 22. Time-averaged bubble size distribution.

size increases, the power-law exponent slightly deviates from −10/3, mainly due to the interaction of large-scale coherent vortices generated by the hydrofoil's wake with the free surface. Large bubbles are dragged deeper into the water as a result of the interaction, which also slows the collapse of large bubbles or cavities and lengthens their residence duration in the water.

Fig. 23 shows the spatial distribution of the time-averaged bubble volume. Fig. 23(a) illustrates the bubble volume distribution along the streamwise direction. For the $h/c = 0.3$、0.5、0.7 and 0.9 conditions, the volume curve first increases to a peak and then slowly decreases. The greater the submergence depth, the higher the peak value. Overall, the $h/c = 1.1$ and $h/c = 1.3$ conditions have smaller volumes along the streamwise direction, with air entrainment starting at $x/c = 5.0$. The $h/c = 1.1$ and $h/c = 1.3$ conditions exhibit somewhat greater volumes downstream in comparison to the others, suggesting that Type-III entrainment is more serious and Type-I entrainment (occurring at $x/c < 5.0$) is absent. Fig. 23(b) shows the air volume distribution along the vertical direction. Peak values are localized in the region $-0.2 < (y-h)/c < 0.0$ in all conditions, and they decrease with increasing submergence depth. In all conditions, the bubble volume approaches zero around $(y-h)/c = -0.6$, indicating that the deeper the submergence, the deeper the bubbles are swept into the water.

The distribution of bubble aggregation structures is closely related to the distribution of coherent structures in the flow field, reflecting the evolution and distribution of turbulent field characteristic scales to some extent. Therefore, the time-averaged bubble number density in the flow field was calculated as follows:

$$\lambda_n(x,y) = \frac{1}{T}\int_t^{t+T} n(x,y)dt \tag{23}$$

where $n(x,y)$ represents the number of instantaneous bubbles detected within the sampling interval $x \le \tilde{x} \le x + \Delta x, y \le \tilde{y} \le y + \Delta y, \Delta x/c = \Delta y/c = 0.1$..

Fig. 24 shows the spatial distribution and number density distribution of bubbles for the $h/c = 0.3$ and $h/c = 1.3$. From the time-averaged spatial distribution, bubbles in the $h/c = 0.3$ condition are mainly concentrated in the leading wave breaking region, with large size bubbles primarily in this region and smaller, dispersed bubbles downstream. For the $h/c = 1.3$ condition, with only Type-III entrainment, bubbles are more widely distributed downstream, with fewer large size bubbles. The number density distribution reveals significant differences between the two conditions. For the $h/c = 0.3$ condition, the highest bubble number density is in the leading wave breaking region ($x/c < 7.0$), with peak values close to the free surface. For the $h/c = 1.3$ condition, bubble number density appears at $x/c > 5.0$, and due to the sinusoidal wave pattern of the free surface, the number density also exhibits a wave-like distribution. The number density peaks are more widespread downstream, indicating that bubbles have split into smaller clusters. Additionally, the number density peak regions for the $h/c = 1.3$ condition are lower than $h/c = 0.3$ condition, also suggesting that Type-III entrainment at greater submergence depths tends to sweep bubbles deeper into the water.

4. Conclusions

In this study, we simulate six conditions with submergence depth ratios of $h/c = 0.3, 0.5, 0.7, 0.9, 1.1$ and 1.3 for a shallowly submerged hydrofoil NACA0012 under incoming flow. Adaptive mesh refinement combined with the CLSVOF interface capturing method is employed to obtain detailed flow structures and air entrainment, including bubble sweep-down. Previous research has focused more on the changes in lift and drag of the hydrofoil at different submergence depths or on flow fields without breaking waves. This study aims to reveal the turbulent field induced by the hydrofoil. Additionally, analyzing bubble entrainment phenomena at different submergence depths is a key objective of this study, which has been lacking in previous research. The following conclusions can be drawn:

1. When the hydrofoil is far from the free surface, the free surface transitions from a continuously breaking two-phase mixture state to a steady-state with sinusoidal wave patterns. At submergence depths

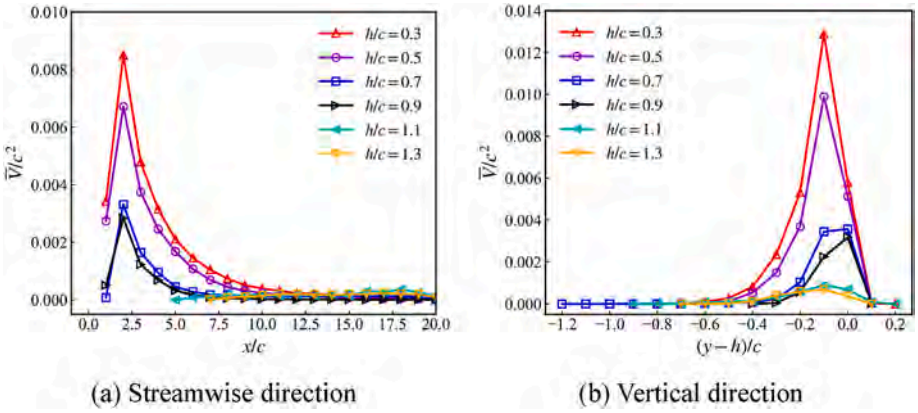

Fig. 23. Time-average bubble volume spatial distribution.

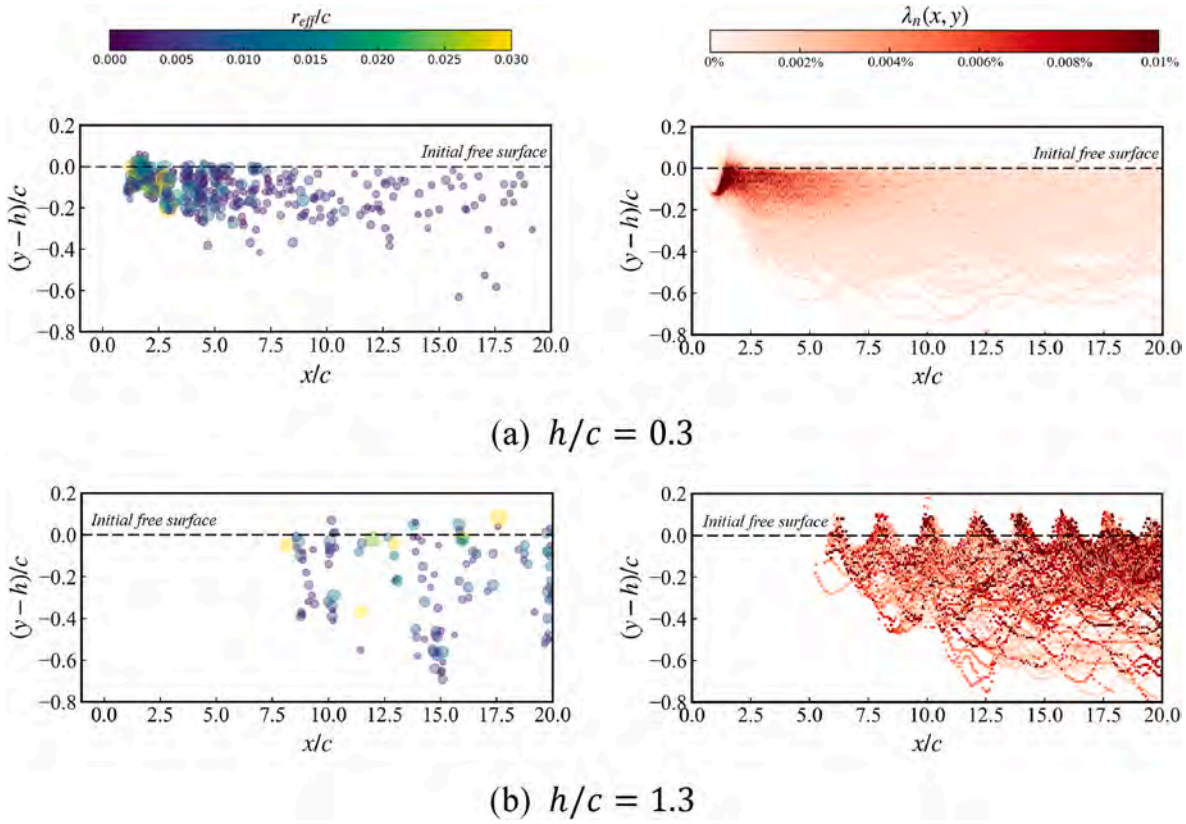

Fig. 24. Bubble space distribution and number density distribution.

of $h/c = 0.9$ and greater, the lift and drag of the hydrofoil remain relatively stable.

2. For the three conditions with severe breaking $h/\ c = 0.3, 0.5,$ and 0.7, the turbulent kinetic energy peaks are concentrated in the leading wave region and the vortex region in the hydrofoil wake. In the one-dimensional distribution of turbulent kinetic energy along streamwise direction, the peak values of $h/c = 0.5$ and $h/\ c = 0.7$ are 60% and 90%, in comparison to the peak value of $h/\ c =\ 0.3$. By analyzing the potential energy flux and kinetic energy flux, it is found that these three conditions dissipate 5.35%, 4.21%, and 3.42% of energy, respectively. Also, due to the vortex wake of the hydrofoil, the turbulent kinetic energy flux exhibits fluctuations in the downstream region.
3. Based on the forms of bubble entrainment at the free surface, this study categorizes bubble entrainment into three types: Type-I, caused by the leading wave breaking due to the obstruction of the near-surface hydrofoil; Type-II, resulting from the interaction between the single vortex structure around bubbles and the free surface; Type-III, caused by the interaction of detached rotating vortex pairs from the hydrofoil's trailing edge with the free surface.
4. Analysis of the spatiotemporal characteristics of entrained bubbles reveals that Type-I entrainment captures the largest volume of bubbles and is the primary source of bubbles in the flow field. Type-II entrainment causes bubbles to be swept to deeper water, increasing their residence time and making them more likely to break into smaller bubbles. In the simulated conditions, with the increase of submergence depth, Type-I entrainment weakens and Type-III entrainment strengthens.

In this study, the numerical investigations of breaking waves and air entrainment induced by a shallowly submerged hydrofoil can bring more references for the application of hydrofoil in ocean engineering, such as fast passenger ferries, marine propeller design in near water conditions and so on. However, the problem is simplified by using two-dimensional simulations and bubble entrainment involves three-dimensional effects. Therefore, in future research, we will study hydrofoils under three-dimensional conditions and consider the effects of hydrofoil pitching motion on free surface disturbances.

CRediT authorship contribution statement

Yuming Shao: Writing – original draft, Visualization, Validation, Methodology, Investigation, Formal analysis, Data curation. **Wentao Wang:** Resources, Investigation, Data curation. **Decheng Wan:** Supervision, Software, Resources, Funding acquisition. **Jianhua Wang:** Writing – review & editing, Supervision, Software, Methodology, Investigation, Conceptualization.

Declaration of competing interest

The authors declare that they have no known competing financial interests or personal relationships that could have appeared to influence the work reported in this paper.

Acknowledgments

This work was supported by the National Natural Science Foundation of China (52131102), to which the authors are most grateful.

References

Ali, A., Karim, M., 2010. Numerical study of free surface effect on the flow around shallowly submerged hydrofoil. Mar 1–6.
Barkley, D., Henderson, R.D., 1996. Three-dimensional Floquet stability analysis of the wake of a circular cylinder. J. Fluid Mech. 322, 215–241.
Blenkinsopp, C.E., Chaplin, J.R., 2010. Bubble size measurements in breaking waves using optical fiber phase detection probes. IEEE J. Ocean. Eng. 35 (2), 388–401.

Carrica, P., Huang, J., Noack, R., Kaushik, D., Smith, B., Stern, F., 2010. Large-scale DES computations of the forward speed diffraction and pitch and heave problems for a surface combatant. Comput. Fluid 39 (7), 1095–1111.
Cetiner, O., Rockwell, D., 2001. Streamwise oscillations of a cylinder in steady current. Part 2. Free-surface effects on vortex formation and loading. J. Fluid Mech. 427, 29–59.
Choi, S.J., Lee, K.H., Gudmestad, O.T., 2015. The effect of dynamic amplification due to a structure's vibration on breaking wave impact. Ocean Eng. 96, 8–20.
Colagrossi, A., Nikolov, G., Durante, D., Marrone, S., Souto-Iglesias, A., 2019. Viscous flow past a cylinder close to a free surface: benchmarks with steady, periodic and metastable responses, solved by meshfree and mesh-based schemes. Comput. Fluid 181, 345–363.
Deane, G.B., Stokes, M.D., 2002. Scale dependence of bubble creation mechanisms in breaking waves. Nature 418 (6900), 839–844.
Deike, L., 2022. Mass transfer at the ocean–atmosphere interface: the role of wave breaking, droplets, and bubbles. Annu. Rev. Fluid Mech. 54, 191–224.
Duncan, J.H., 1983. The breaking and non-breaking wave resistance of a two-dimensional hydrofoil. J. Fluid Mech. 126, 507–520.
Erinin, M.A., Liu, C., Wang, S.D., Liu, X., Duncan, J.H., 2023a. Plunging breakers. Part 2. Droplet generation. J. Fluid Mech. 967, A36.
Erinin, M.A., Liu, X., Wang, S.D., Duncan, J.H., 2023b. Plunging breakers. Part 1. Analysis of an ensemble of wave profiles. J. Fluid Mech. 967, A35.
Guo, C., Ji, M., Han, Y., Liu, T., Wu, Y., Kuai, Y., 2023. Numerical simulation of the horizontal rotating cylinder and the air entrainment near the free surface. Phys. Fluids 35 (9).
Hashemi, M., Shalbaf, S., Jadidi, M., Dolatabadi, A., 2023. Effects of gas viscosity and liquid-to-gas density ratio on liquid jet atomization in crossflow. AIP Adv. 13 (3).
Hendrickson, K., Yu, X., Yue, D.K., 2022. Modelling entrainment volume due to surface-parallel vortex interactions with an air–water interface. J. Fluid Mech. 938, A12.
Hendrickson, K., Yue, D.K.P., 2019. Structures and mechanisms of air-entraining quasi-steady breaking ship waves. J. Ship Res. 63 (2), 69–77.
Hu, Y., Liu, C., Hu, C., Wan, D., 2021. Numerical investigation of flow structure and air entrainment of breaking bow wave generated by a rectangular plate. Phys. Fluids 33 (12).
Hu, Y., Liu, C., Zhao, M., Hu, C., 2023. High-fidelity simulation of an aerated cavity around a surface-piercing rectangular plate. Physical Review Fluids 8 (4), 044003.
Jin, Q., Hudson, D., Temarel, P., Price, W.G., 2021. Turbulence and energy dissipation mechanisms in steady spilling breaking waves induced by a shallowly submerged hydrofoil. Ocean Eng. 229, 108976.
Kang, D., Ghosh, S., Reins, G., Koo, B., Wang, Z., Stern, F., 2012. Impulsive plunging wave breaking downstream of a bump in a shallow water flume—Part I: experimental observations. J. Fluid Struct. 32, 104–120.
Karim, M.M., Prasad, B., Rahman, N., 2014. Numerical simulation of free surface water wave for the flow around NACA 0015 hydrofoil using the volume of fluid (VOF) method. Ocean Eng. 78, 89–94.
Kennell, C., Plotkin, A., 1984. A second-order theory for the potential flow about thin hydrofoils. J. Ship Res. 28 (1), 55–64.
Li, Z., Liu, C., Wan, D., Hu, C., 2021. High-fidelity simulation of a hydraulic jump around a surface-piercing hydrofoil. Phys. Fluids 33 (12).
Li, Z., Zhang, X.S., Wan, D.C., 2022. Research progress on the hydrodynamic performance of water-air-bubble mixed flows around a ship. J. Hydrodyn. 34 (2), 171–188.
Limare, A., Popinet, S., Josserand, C., Xue, Z., Ghigo, A., 2023. A hybrid level-set/embedded boundary method applied to solidification-melt problems. J. Comput. Phys. 474, 111829.
Liu, S., Wang, H., Bayeul-Lainé, A.C., Li, C., Katz, J., Coutier-Delgosha, O., 2023. Wave statistics and energy dissipation of shallow-water breaking waves in a tank with a level bottom. J. Fluid Mech. 975, A25.
Mallat, B., Germain, G., Gaurier, B., Druault, P., Billard, J.Y., 2018. Experimental study of the bubble sweep-down phenomenon on three bow designs. Ocean Eng. 148, 361–375.
Miller, M., Nennstiel, T., Duncan, J.H., Dimas, A.A., Pröstler, S., 1999. Incipient breaking of steady waves in the presence of surface wakes. J. Fluid Mech. 383, 285–305.
Mossa, M., 2008. Experimental study of the flow field with spilling type breaking. J. Hydraul. Res. 46 (Suppl. 1), 81–86.
Mostert, W., Popinet, S., Deike, L., 2022. High-resolution direct simulation of deep water breaking waves: transition to turbulence, bubbles and droplets production. J. Fluid Mech. 942, A27.
Murai, Y., Sakamaki, H., Kumagai, I., Park, H.J., Tasaka, Y., 2020. Mechanism and performance of a hydrofoil bubble generator utilized for bubbly drag reduction ships. Ocean Eng. 216, 108085.
Ni, Z., Dhanak, M., Su, T.C., 2019. Performance of a slotted hydrofoil operating close to a free surface over a range of angles of attack. Ocean Eng. 188, 106296.
Ni, Z., Dhanak, M., Su, T.C., 2021. Performance of a hydrofoil operating close to a free surface over a range of angles of attack. Int. J. Nav. Archit. Ocean Eng. 13, 1–11.
Olivieri, A., Pistani, F., Mascio, A.D., 2003. Breaking wave at the bow of a fast displacement ship model. J. Mar. Sci. Technol. 8 (2), 68–75.
Olivieri, A., Pistani, F., Wilson, R., Campana, E.F., Stern, F., 2007. Scars and vortices induced by ship bow and shoulder wave breaking. J. Fluid Eng. 129 (11), 1445–1459.
Pernod, L., Sacher, M., Wackers, J., Augier, B., Bot, P., 2023. Free-surface effects on two-dimensional hydrofoils by RANS-VOF simulations. Journal of Sailing Technology 8 (1), 24–38.
Popinet, S., 2009. An accurate adaptive solver for surface-tension-driven interfacial flows. J. Comput. Phys. 228 (16), 5838–5866.
Popinet, S., 2015. A quadtree-adaptive multigrid solver for the Serre–Green–Naghdi equations. J. Comput. Phys. 302, 336–358.
Popinet, S., 2018. Numerical models of surface tension. Annu. Rev. Fluid Mech. 50, 49–75.
Prasad, B., Hino, T., Suzuki, K., 2015. Numerical simulation of free surface flows around shallowly submerged hydrofoil by OpenFOAM. Ocean Eng. 102, 87–94.
Rao, A., Leontini, J., Thompson, M.C., Hourigan, K., 2013. Three-dimensionality in the wake of a rotating cylinder in a uniform flow. J. Fluid Mech. 717, 1–29.
Schwartz, P., Barad, M., Colella, P., Ligocki, T., 2006. A Cartesian grid embedded boundary method for the heat equation and Poisson's equation in three dimensions. J. Comput. Phys. 211 (2), 531–550.
Sheridan, J., Lin, J.C., Rockwell, D., 1997. Flow past a cylinder close to a free surface. J. Fluid Mech. 330, 1–30.
Sykes, T.C., Cimpeanu, R., Fudge, B.D., Castrejón-Pita, J.R., Castrejón-Pita, A.A., 2023. Droplet impact dynamics on shallow pools. J. Fluid Mech. 970, A34.
Wang, J., Ren, Z., Wan, D., 2020. Study of a container ship with breaking waves at high Froude number using URANS and DDES methods. J. Ship Res. 64 (4), 346–356.
Wang, Z., Yang, J., Stern, F., 2016. High-fidelity simulations of bubble, droplet and spray formation in breaking waves. J. Fluid Mech. 792, 307–327.
Wu, G.X., Taylor, R.E., 1995. Time stepping solutions of the two-dimensional nonlinear wave radiation problem. Ocean Eng. 22 (8), 785–798.
Yang, Y., Hu, Y., Liu, C., Gao, R., Hu, C., 2023. Wake and air entrainment properties of transom stern over a wide range of Froude numbers. Phys. Fluids 35 (6).